

# Microwave-Assisted Synthesis of $\text{Pd}_x\text{Au}_{100-x}$ Alloy Nanoparticles: A Combined Experimental and Theoretical Assessment of Synthetic and Compositional Effects upon Catalytic Reactivity

Pranaw Kunal,<sup>†</sup> Hao Li,<sup>†</sup> Beth L. Dewing,<sup>†,§</sup> Liang Zhang,<sup>†,||</sup> Karalee Jarvis,<sup>‡</sup> Graeme Henkelman,<sup>\*,†</sup> and Simon M. Humphrey<sup>\*,†</sup>

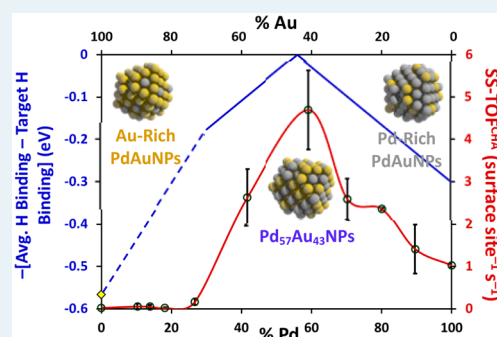
<sup>†</sup>Department of Chemistry, The University of Texas at Austin, 6.336 Norman Hackerman Building, 100 E 24th St. Stop A1590, Austin, Texas 78712-1224, United States

<sup>‡</sup>Texas Materials Institute, The University of Texas at Austin, 204 E. Dean Keeton St. Stop C2201, Austin, Texas 78712-1591, United States

## S Supporting Information

**ABSTRACT:**  $\text{Pd}_x\text{Au}_{100-x}$  nanoparticle (NP) catalysts with well-defined morphologies and compositions can be rapidly prepared using a simple microwave-assisted synthetic approach. Common Pd(II) and Au(III) precursors are coreduced in ethylene glycol to give small and nearly monodisperse ( $2.5 \pm 0.6$  nm) NPs with homogeneously alloyed structures in less than 300 s at 150 °C. A comparison of the nucleation and growth processes responsible for the formation of PdAuNPs by microwave and conventional methods revealed faster and more reproducible product formation under microwave-assisted heating. Pd-rich NPs were rapidly formed, into which Au atoms were subsequently incorporated to give the alloyed NPs. The value of  $x$  in the  $\text{Pd}_x\text{Au}_{100-x}$  NPs obtained can be finely controlled, allowing the surface electronic structure of the NPs to be broadly tuned. This permits model heterogeneous reaction studies, in which catalytic reactivity can be directly related to Pd:Au composition. Vapor-phase alkene hydrogenation studies using a series of PdAuNPs with varying compositions revealed that  $\text{Pd}_{59}\text{Au}_{41}$  NPs were catalytically the most active. Detailed theoretical studies of the entire hydrogenation reaction catalyzed at randomly alloyed PdAu surfaces were performed using a density functional theory (DFT) approach. Local ensemble effects and longer range electronic effects in the alloys were considered, leading to a prediction for optimal hydrogenation activity by  $\text{Pd}_{57}\text{Au}_{43}$  NPs. PdAuNPs obtained from microwave-assisted syntheses were also found to be more highly active than analogous NPs prepared conventionally. Quantitative solution-state  $^1\text{H}$  NMR studies suggest that significantly less PVP was incorporated into PdAuNPs synthesized under microwave heating.

**KEYWORDS:** alloy nanoparticles, microwave synthesis, palladium–gold alloys, heterogeneous catalysis, density functional theory (DFT), hydrogenation



## 1. INTRODUCTION

The scalable and controlled synthesis of bimetallic noble-metal nanoparticles (MNPs) with well-defined surface structures and compositions is of importance for a wide range of industrial applications. Alloys consisting of two or more metals are widely employed in large-scale catalytic processes that generate valuable commodity chemicals from raw feedstocks.<sup>1–4</sup> The catalytic properties of metal alloys are commonly superior to what is observed for the corresponding pure metals.<sup>5–11</sup> The electronic structure of alloys can be broadly modulated as a function of synthetic control of composition. This allows for tuning and optimization of surface chemical reactivity via charge transfer,<sup>12,13</sup> d band mixing,<sup>14,15</sup> and lattice strain effects.<sup>15</sup> On a more localized level, geometric ensemble effects (dependent on specific arrangements of discrete groups of atoms) are also known to be important in providing sites with

particularly beneficial catalytic reactivity and/or selectivity.<sup>13,15–18</sup>

Experimental analysis of the relationships between the relative composition of bimetallic alloys and the resulting catalytic behavior provides important information that can be compared to theoretical models of electronic structure and surface reactivity. In turn, these results can be exploited to predict more general trends in reactivity and to direct the future syntheses of catalysts with desired properties. Such studies require access to highly defined model catalysts. The majority of alloy catalysts currently employed in industry are prepared on a large scale via simple colloidal processes. An example is incipient wetness impregnation to incorporate molecular metal

Received: April 7, 2016

Revised: June 13, 2016

Published: June 14, 2016

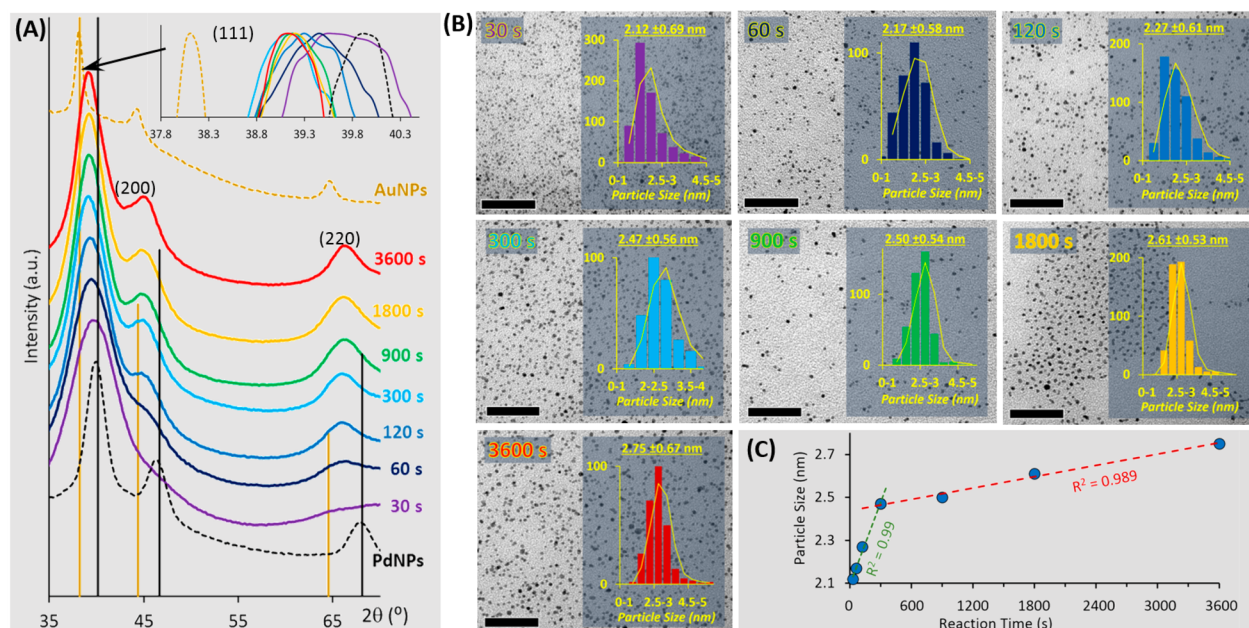


**Figure 1.** (A) Evolution of PXRD patterns as a function of time in the formation of Pd<sub>50</sub>Au<sub>50</sub>NPs. PXRD patterns obtained for PdNPs and AuNPs (dashed lines) are compared to the theoretical peak positions (Pd, black; Au, gold). Inset: expansion of the peak maxima region corresponding to the (111) reflection. (B) TEM images for the products at the same time intervals studied by PXRD. Insets: NP size histograms obtained from multiple images. Yellow curves overlaid on the histograms correspond to a two-point moving average. Scale bars are 50 nm. (C) Relationship between average NP size and reaction time.  $R^2$  values are shown for the two straight-line fits applied to the data.

precursors into support media, followed by in situ coreduction. This type of approach offers limited synthetic control, yielding composite materials in which the active metal species have a significant range of structures and compositions, usually with nanometer dimensions. The different metals may exist as separate entities or as intrinsically alloyed particles. Over long reaction lifetimes, the atomic arrangement of atoms in nanosized bimetallic catalysts may sometimes evolve (e.g., by enrichment of one metal near the surface or by complete segregation).<sup>19–21</sup> Therefore, the most important active catalytic sites in such bimetallic catalysts are difficult to study, which hampers an in-depth understanding of structure–reactivity relationships. The ability to identify economical and realistically scalable routes for the synthesis of well-defined bimetallic catalysts with thermodynamically persistent structures is therefore of interest.

An excellent example is provided by bimetallic catalysts based on palladium and gold: Pd/Au catalysts are versatile and are widely used in a variety of large-scale industrial processes, including vinyl acetate monomer (VAM) synthesis,<sup>6,22</sup> direct hydrogen peroxide synthesis,<sup>23–25</sup> and alcohol oxidations.<sup>26–30</sup> Empirically, catalysts with approximate 2:1 Pd:Au ratios result in optimal reactivity for the reactions stated above. However, the underlying reasons for the observed relationships between Pd:Au compositions and catalytic activities are still not fully understood and are the subject of continued debate.<sup>31–34</sup> Extensive studies by Goodman and co-workers elucidated the beneficial effects of controlled incorporation of Au into Pd, via model studies on single-crystal surfaces.<sup>6,22,35,36</sup> They showed that geometric ensemble effects were highly important, while isolated Au atoms were also able to inhibit the formation of unwanted byproducts that otherwise resulted in deactivation of Pd sites.

We have recently shown that microwave irradiation ( $\mu$ wI) can be exploited to obtain noble-metal alloy nanoparticles

(NPs) with highly tunable compositions, in shorter reaction times, and at significantly lower temperatures than are required using conventional heating (convective; CvH) methods.<sup>37</sup> Alloy NPs based on classically immiscible combinations of metals such as RhAg and RhAu can also be obtained by coinjection of metal halide precursors under  $\mu$ wI.<sup>38</sup> It is comparatively trivial to prepare alloy NPs based on miscible metals under  $\mu$ wI. For example, Pd<sub>x</sub>Au<sub>100–x</sub>NPs can be prepared with broadly tunable compositions and highly defined morphologies by an optimized  $\mu$ w-assisted method. From a practical standpoint,  $\mu$ w-assisted chemistry is also more easily scalable than conventional batch NP syntheses, because it can be conducted under continuous flow. In comparison to the relatively large number of methods available for the in situ synthesis of supported PdAu alloy NPs, there are many fewer examples of convenient methods to prepare small (<3 nm) unsupported PdAuNPs with finely tunable compositions.<sup>26,33</sup> The potential benefits provided by rapid  $\mu$ wI heating in the synthesis of metallic NPs have surprisingly remained unexplored for PdAu alloys until now.

We show here that metal precursor coinjection into hot ethylene glycol under  $\mu$ wI affords PdAuNPs with finely controllable sizes and compositions. When they are directly compared to similar syntheses under CvH, the  $\mu$ w-prepared PdAuNPs are more uniformly alloyed in shorter reaction times, are more monodisperse, and are more highly active in the low-temperature heterogeneous hydrogenation of alkenes. Assessment of catalytic reactivity as a function of composition using alkene hydrogenation as a model reaction provides fundamental information applicable to other catalytic reaction types. The experimentally observed trends in activity as a function of Pd<sub>x</sub>Au<sub>100–x</sub> composition have been compared to a model of the alkene hydrogenation reaction derived by density functional theory (DFT). Consideration of surface ensemble effects and surface binding energies for each discrete catalytic step provides results that predict a maximum hydrogenation activity for

randomly alloyed NPs of composition  $\text{Pd}_{57}\text{Au}_{43}$ , which is in close agreement with experimental observations.

## 2. RESULTS AND DISCUSSION

**2.1. Microwave versus Conventional Heating in the Polyol Synthesis of  $\text{Pd}_{50}\text{Au}_{50}$ NPs.** To begin, the synthesis of randomly alloyed  $\text{PdAu}$ NPs with  $\mu\text{w}$ -assisted heating was investigated, optimized, and then compared to the products obtained from identical reactions under CvH. Our initial studies involved the optimization of reaction conditions for the reproducible synthesis of randomly alloyed  $\text{PdAu}$ NPs by  $\mu\text{wI}$ , using 1:1 as the target Pd:Au composition. The method employed was adapted from our previous work.<sup>37,38</sup> Briefly, the metal precursors ( $\text{K}_2\text{PdCl}_4$  and  $\text{HAuCl}_4$  hydrates) were codissolved in ethylene glycol and injected at a controlled rate via syringe pump, directly into an ethylene glycol (EG) solution of poly(*N*-vinylpyrrolidone) (PVP) and sodium borohydride, which was already held at 150 °C (see the Experimental Section and Supporting Information). All  $\mu\text{wI}$  reactions were performed in a CEM MARS-5 acid digestion reactor, which was modified to accommodate the same configuration of glassware used in otherwise identical experiments performed on a benchtop under CvH (by direct immersion in an oil bath).

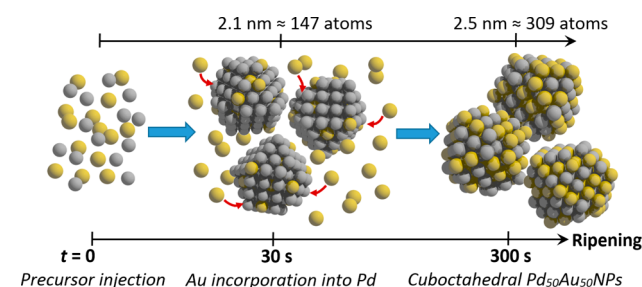
$\text{Pd}_x\text{Au}_{100-x}$  alloys are supposedly miscible for all values of  $x$ .<sup>39</sup> However, the exact mechanism of nucleation and growth of randomly alloyed bimetallic NPs from molecular ions in solution is the subject of continued debate.<sup>40,41</sup> From our detailed studies presented here, there are subtle yet clear differences in the nucleation of  $\text{Pd}_x\text{Au}_{100-x}$ NPs, on the basis of the mode of heating. Our observations imply that the kinetics of the nucleation process are altered by dipolar heating, because the observed thermodynamic products are smaller and more monodisperse. When a 1:1 molar ratio of Pd(II) and Au(III) ions was coinjected into hot EG/PVP/ $\text{NaBH}_4$  under  $\mu\text{wI}$ , the solution appeared to darken immediately, suggesting rapid nucleation. However, time-dependent powder X-ray diffraction analysis (PXRD; Figure 1A) of the products revealed more detailed mechanistic insights. For reaction times as short as 30 s after completion of injection of the precursors, the (111) reflection was located at  $2\theta_{\text{max}} = 39.6^\circ$ , which is similar to what should be expected for PdNPs. However, upon continued heating, this peak steadily shifted to  $2\theta_{\text{max}} = 39.1^\circ$ , which corresponds exactly to the theoretical  $2\theta_{\text{max}}$  value for the (111) reflection in  $\text{Pd}_{50}\text{Au}_{50}$ NPs (calculated using lattice parameters obtained from the CCDC;<sup>42</sup> Pd  $40.1^\circ$ , Au  $38.2^\circ$ ). In comparison, when pure PdNPs and AuNPs were synthesized under otherwise identical  $\mu\text{wI}$  conditions, the observed  $2\theta_{\text{max}}$  values for the (111) reflection after 300 s of heating were  $39.9^\circ$  and  $38.1^\circ$ , respectively (Figure 1A, inset). After 300 s of heating, no further changes were observed in the PXRD spectra of the alloy NPs as a result of prolonged  $\mu\text{wI}$  up to 1 h.

Analysis of the evolution of  $\text{Pd}_{50}\text{Au}_{50}$ NP size as a function of heating time revealed a direct relationship to the PXRD-based observations. Transmission electron microscopy (TEM) was used to measure the average NP size at the same reaction times studied by PXRD (Figure 1B). This revealed a distinct two-stage growth process: particle growth was fast within the first 300 s of reaction but very slow thereafter (Figure 1C). The NPs were nearly monodisperse at all phases of growth, and the predominant morphology was cuboctahedral. This assumption is supported by the ratio of (111):(200) diffraction intensities observed by PXRD (Table S1 in the Supporting Information).

At short reaction times (30 s), the initial seed NPs were  $2.12 \pm 0.7$  nm, which corresponds closely to cuboctahedral clusters with the so-called “magic number” of 147 atoms (theoretical size 1.93 nm for Pd).<sup>43</sup> At longer reaction times (>300 s), the NPs had grown to  $2.47 \pm 0.6$  nm, which corresponds to the next largest magic number cluster, containing 309 atoms (theoretical size 2.53 nm for 1:1 Pd:Au). The subsequent slow and linear rate of growth between 300 and 3600 s is most consistent with what should be expected for simple Ostwald ripening (size-focusing) processes.<sup>44,45</sup> UV–vis spectroscopy showed that the characteristic absorption due to the surface plasmon excitation for AuNPs (ca. 528 nm) was not evident in any of the NPs formed at short or longer reaction times (Figure S2 in the Supporting Information). Equally, the UV–vis spectrum for pure PdNPs did not show an observable plasmonic absorption peak, which indicated that Au(0) was always intrinsically alloyed with Pd(0) and that AuNPs were never formed.

Collectively, these data suggest that, under  $\mu\text{w}$  irradiation, the first species to form were small Pd-rich NPs, into which Au atoms were subsequently incorporated during the first 300 s of the reaction. It has been previously reported that Au(III) can be autocatalytically reduced by Pd(0), including at the surfaces of PdNPs.<sup>46</sup> In our experiments, the Pd and Au precursor ions appeared to be fully consumed and reduced to form  $\text{Pd}_{50}\text{Au}_{50}$ NPs in less than 300 s at 150 °C. This arrangement was also persistent upon further heating. Scheme 1 shows the

**Scheme 1. Proposed Mechanism for the Formation of  $2.47 \pm 0.6$  nm  $\text{Pd}_{50}\text{Au}_{50}$ NPs under  $\mu\text{wI}$**



proposed formation mechanism of  $\text{Pd}_{50}\text{Au}_{50}$ NPs under  $\mu\text{wI}$ . Analysis of the bulk products obtained after 300 s by inductively coupled plasma-mass spectroscopy (ICP-MS) indicated that the actual relative composition was closer to  $\text{Pd}_{42}\text{Au}_{58}$  (Table 1), while elemental line scans of individual particles performed by energy-dispersive X-ray spectroscopy (EDS) gave an average composition of  $\text{Pd}_{45}\text{Au}_{55}$  (Table 1).

Next, we probed the effects of  $\mu\text{wI}$ , by applying the optimized reaction conditions for the synthesis of  $\text{Pd}_{50}\text{Au}_{50}$ NPs under CvH via immersion in an oil bath. Figure 2A shows a comparison of NP size and the extent of alloying for CvH (red triangles) versus  $\mu\text{wI}$  (blue circles) as a function of reaction time. Under CvH, there was less definition between NP nucleation and growth stages. In fact, the average NP size appeared to increase constantly for the duration of the reaction (Figure 2A, top). TEM of the products showed the formation cuboctahedral NPs (Table S1 and Figure S3 in the Supporting Information) that were more polydisperse in comparison to  $\mu\text{wI}$  (Figure 2B). However, NP nucleation occurred more slowly under CvH, while ripening was more evident upon prolonged heating. PXRD analysis of the CvH products also suggested that the initial seeds were Pd rich, but after 900 s,

Table 1. Average PdAuNP Composition Values

target composition (%)		composition by ICP-MS (%)		composition by EDS (%)		composition by XPS (%)	
Pd	Au	Pd	Au	Pd	Au	Pd	Au
91	9	90	10	91	9	90	10
84	16	80	20	80	20	86	14
75	25	71	29	74	26	69	31
67	33	59	41	61	39	66	34
50	50	42	58	45	55	55	45
33	67	27	73	32	68	42	58
25	75	18	82	23	77	34	66
16	84	14	86	15	85	30	70
9	91	10	90	13	87	26	74

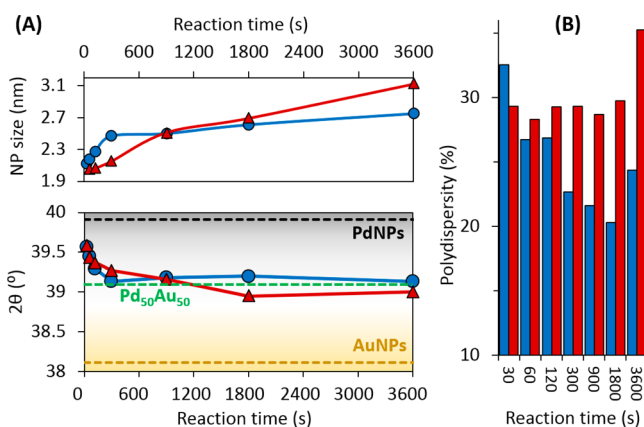


**Figure 2.** (A) Comparison of Pd<sub>50</sub>Au<sub>50</sub>NP average size (top) and extent of alloying (bottom) as a function of reaction time for CvH (red) and μwI (blue). (B) Comparison of time-dependent NP polydispersity versus heating method.

both Pd and Au were evenly incorporated into randomly alloyed NPs (Figure 2A, bottom). ICP-MS analysis of the products of CvH gave a bulk composition of Pd<sub>39</sub>Au<sub>61</sub>. The most important difference in this case between μwI and CvH methods was the rate of nucleation and growth, which was clearly faster under μwI. This correlates directly to what has been observed for other NP syntheses: favorable coupling of μwI to polar metal species and organic solvents (e.g., EG) results in rapid energy transfer and the generation of nanosized “hotspots”, which promote more rapid NP nucleation and growth.<sup>47,48</sup> The lack of extensive ripening by μwI in comparison to CvH at longer reaction times suggests that the metal precursors were more effectively and more rapidly consumed under μwI. The observation that the μw-prepared NPs were significantly more monodisperse should also disfavor NP ripening, which generally occurs via the sacrificial redissolution of smaller NPs (Figure 2B).

Although the Pd<sub>50</sub>Au<sub>50</sub>NPs obtained from μwI did not ripen substantially with increased heating time, it was nonetheless possible to use these 2.5 nm NPs as seeds for subsequent controlled overgrowth, to obtain larger alloyed NPs. This was achieved by coaddition of further Pd(II) and Au(III) precursors, directly into the Pd<sub>50</sub>Au<sub>50</sub>NP suspensions obtained after 300 s of initial heating. Conveniently, it was not necessary to isolate the intermediate NPs, and additional NaBH<sub>4</sub> reducing agent was not required in this step. Overgrowth was achieved at 150 °C via injection of additional metal precursors (1:1 Pd:Au molar ratio) at a rate much slower than that employed in the

initial injection (0.8 versus 12 mmol h<sup>-1</sup>, respectively); the NPs were then heated for a further 300 s after the second addition had completed. The slower injection rate ensured that the new precursors were exclusively added to the existing NPs, since the concentration of free ions in solution never reached the supersaturation threshold required for nucleation of new seeds. Importantly, all analyses showed that the newly deposited overlayers also consisted of random PdAu alloys, and regions of pure Pd or Au were not deposited (Figure S4 in the Supporting Information). The total molar amounts of additional precursors that were added also shared a linear relationship with the resulting average Pd<sub>50</sub>Au<sub>50</sub>NP size. This indicated that the growth was mainly isotropic in nature, occurring at similar rates for all seeds. For example, analysis of the products by PXRD and TEM (Figures S4 and S5 in the Supporting Information) obtained after addition of 0.05 and 0.10 mmol of further metal precursors showed no apparent change in the bulk composition, but the average NP size was increased to 3.26 ± 0.75 and 3.69 ± 0.98 nm, respectively.

The dependence of NaBH<sub>4</sub> concentration on the nucleation of the 2.47 ± 0.56 nm Pd<sub>50</sub>Au<sub>50</sub>NPs was also investigated. Borohydride is often employed in the synthesis of metallic NPs of the more inert noble metals in order to facilitate reduction of the ionic precursors.<sup>49–52</sup> In contrast, other metal cations can be reduced at relatively low temperatures by solvents (e.g., by alcohols or polyols). Under the synthetic conditions employed in our work, K<sub>2</sub>PdCl<sub>4</sub> was rapidly reduced under μwI at 150 °C by EG alone, to give 4.8 ± 0.7 nm PdNPs. In contrast, HAuCl<sub>4</sub> was not reduced under the same conditions, even after 30 min of heating. Following this supposition, when no NaBH<sub>4</sub> was employed in the μwI-assisted reaction between Pd(II) and Au(III), only large and polydisperse (6.3 ± 4.0 nm) NPs were obtained after 300 s of μwI. As the amount of NaBH<sub>4</sub> was increased, the NPs obtained after the same reaction time became smaller and more monodisperse and were closer to the target composition of Pd<sub>50</sub>Au<sub>50</sub>. Addition of 6 equiv of NaBH<sub>4</sub> (with respect to Au(III)) was found to be optimal in this instance; there appeared to be no noticeable improvement in the products obtained by the addition of increased amounts of NaBH<sub>4</sub>. It should be noted that PXRD analysis and elemental dispersive X-ray analysis (EDS) line scans of individual 6.3 ± 4.0 nm NPs obtained in the absence of NaBH<sub>4</sub> showed that these were predominantly alloyed, albeit with some degree of Pd–Au segregation (Figures S6, S7, and S22 in the Supporting Information). By consideration of the nucleation and growth model already defined from our detailed time-dependent studies (Scheme 1) it would be reasonable to assume that, in the absence of NaBH<sub>4</sub>, the only means of Au(III) reduction would be via autocatalytic reduction and subsequent incorporation into preformed 4.8 nm PdNPs. In turn, this would result in the formation of even larger, polydisperse PdAuNPs.

**2.2. Rapid μwI-Assisted Synthesis of Pd<sub>x</sub>Au<sub>100-x</sub>NPs (x = 10–90).** The optimized μwI-assisted method was then applied to the synthesis of Pd<sub>x</sub>Au<sub>100-x</sub>NPs. Our initial crude assumption was that *x* should be simply dictated by the relative molar amounts of metal precursors used in a given synthesis. For metals with broad miscibility, it is commonly most difficult to achieve fine control in the preparation of alloyed NPs with extremely biased compositions (e.g., NPs that are very rich in either Pd or Au). We attempted to prepare a family of PdAuNPs with nominal target compositions of 10:1, 5:1, 3:1, 2:1, 1:2, 1:3, 1:5, and 1:10 (corresponding to *x* = 91, 84, 75, 67, 33, 25, 16, 9). In all experiments, the total molar amount of Pd

+ Au was kept constant; the reaction conditions and isolation methods were otherwise identical to those described in section 2.1 for the synthesis of 1:1 PdAuNPs. The bulk Pd:Au compositions of the products obtained after 300 s under  $\mu$ wI were examined by PXRD, ICP-MS, EDS, and X-ray photoelectron spectroscopy (XPS) (Figures 3 and 4 and Table 1) as

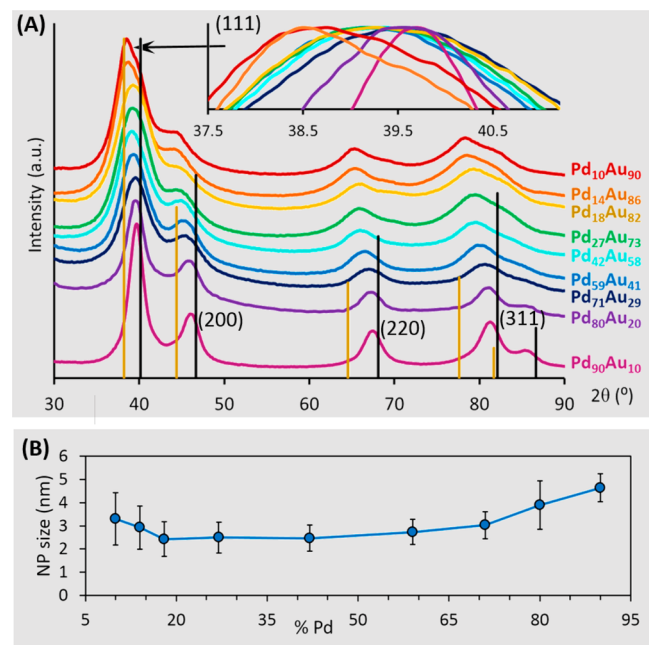


**Figure 3.** (A) PXRD patterns for  $\text{Pd}_x\text{Au}_{100-x}$ NPs showing peak shifting as a function of composition. Inset: expansion of (111) peak maxima region. (B) Trend in average  $\text{Pd}_x\text{Au}_{100-x}$ NP size versus composition (error bars show standard deviation to  $1\sigma$ ).

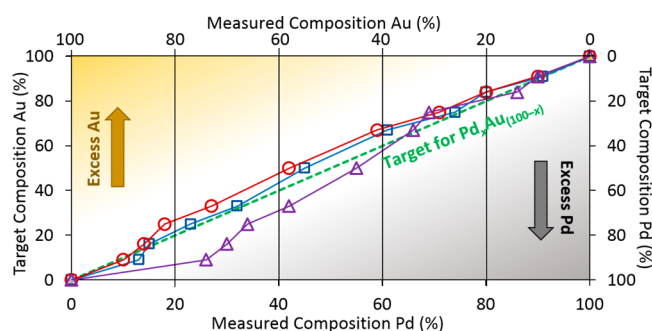


**Figure 4.** Comparison of measured  $\text{Pd}_x\text{Au}_{100-x}$ NP compositions obtained from different analytical methods applied to the bulk products versus the nominal target composition (green dashed line) on the basis of molar ratios of Pd(II) and Au(III) precursors employed in the syntheses: ICP-MS (red circles); EDS (blue squares); XPS (purple triangles).

well as TEM and UV–vis spectrophotometry (Figures S8 and S9 in the Supporting Information). The peak positions in the PXRD spectra of  $\text{Pd}_x\text{Au}_{100-x}$ NPs showed shifts consistent with the changing value of  $x$  across the entire range of compositions studied: as  $x$  increased, the peak maxima smoothly shifted toward the  $2\theta$  value expected for pure PdNPs (Figure 3A). The values of  $x$  shown in Figure 3 were obtained from ICP-MS analysis, to permit a realistic comparison of the observed PXRD patterns to the actual corresponding bulk compositions (vide infra). Analysis of the average  $\text{Pd}_x\text{Au}_{100-x}$ NP size by TEM

suggested that all products with intermediate compositions in the range  $x = 18$ –71 were very similar in size and monodispersity to the  $\text{Pd}_{42}\text{Au}_{58}$ NPs (Figure 3B). The average NP size increased slightly, in a linear fashion, toward the most outlying compositions studied ( $x = 10, 90$ ; determined by ICP-MS). This is in agreement with the observation that pure PdNPs and AuNPs obtained under the same reaction conditions were always larger than any of the alloy NPs. One plausible explanation for this trend is that the surfaces of similarly sized NPs are more stable (i.e., more well passivated by PVP) when Pd and Au were alloyed.

EDS is useful to probe the elemental composition of individual  $\text{Pd}_x\text{Au}_{100-x}$ NPs and to confirm whether this is commensurate with measurements of the bulk. In this work, EDS analysis of all of the  $\text{Pd}_x\text{Au}_{100-x}$ NPs gave close agreement with ICP-MS data for all compositions (Figure 4 and Table 1). Both analytical methods suggested that the actual  $\text{Pd}_x\text{Au}_{100-x}$ NPs obtained were also well matched with the target compositions, consistently containing proportions of Au only marginally higher than expected. For the purposes of using defined PdAuNPs as models of heterogeneous catalysts, it is important to discern the extent of structural uniformity of the NPs. More specifically, information about surface composition is vital to permit an understanding of trends in reactivity. While PXRD, EDS, and TEM analyses were able to confirm that randomly alloyed arrangements of Pd and Au are prevalent over segregated metals, it is more difficult to ascertain from these measurements whether individual NPs were homogeneous throughout—or if the surfaces were enriched in one particular metal. It is well known that alloys can undergo spontaneous restructuring in the presence of particular adsorbates, driven by preferential adsorbate binding to one metal over another. In turn, this induces segregation at (or near) the surface.<sup>19,20,53–57</sup> By the same principle, core–shell NPs have been observed to undergo structural inversion in response to the chemical nature of their external environment.<sup>58–60</sup> In the case of Pd and Au, Au(0) is more resistant to oxidation and is chemically less reactive than Pd(0) ( $\text{Au} \rightarrow \text{Au}^+ + \text{e}^- = -1.68 \text{ V}$ ;  $\text{Pd} \rightarrow \text{Pd}^{2+} + 2\text{e}^- = -0.987 \text{ V}$ ).<sup>61</sup>

X-ray photoelectron spectroscopy (XPS) has the ability to provide more surface specific information in the case of PVP-capped  $\text{Pd}_x\text{Au}_{100-x}$ NPs. In general, emitted photoelectrons observed in XPS emanate from only the top 5–10 nm of a given substrate.<sup>62,63</sup> For small (2–5 nm) NPs, it might therefore be expected that the entire structures are uniformly probed by XPS. However, the additional thickness of any NP surface passivation agents must also be considered. The  $\text{Pd}_x\text{Au}_{100-x}$ NPs are capped with PVP in their native state; we have previously shown for PVP-capped Au-core Rh-shell NPs that as few as 4 monolayers of Rh atoms in the shells were able to totally obscure the Au cores from the incident X-rays.<sup>64</sup> In the present work, an interesting general trend was found by direct comparison of XPS-derived elemental composition data to those obtained from EDS and ICP-MS measurements of the same samples: the percent of Pd was consistently higher by XPS than by the other methods (Figure 4, purple triangles). The most obvious explanation for the disparity in these data is that there was slight enrichment of Pd toward the surfaces of the  $\text{Pd}_x\text{Au}_{100-x}$ NPs. Given that the samples were analyzed in their native (air-exposed) state, this type of enrichment is reasonable, since Pd surface sites would be more susceptible to oxidation than Au. Pd also forms stronger dative interactions toward PVP monomers than Au does.<sup>65–67</sup> An alternative

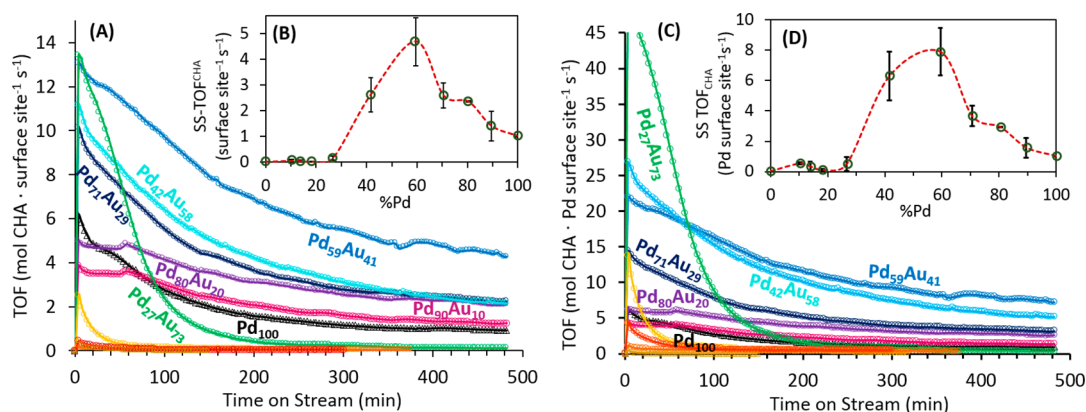


**Figure 5.** (A) Comparison of vapor-phase single pass TOFs for the catalytic hydrogenation of CHE at 298 K by SiO<sub>2</sub>-supported Pd<sub>x</sub>Au<sub>100-x</sub>NPs (color coded by composition as shown in Figure 3A), PdNPs (black triangles), and AuNPs (gold triangles), normalized per total NP surface. (B) Reactivity curve showing the corresponding relationship between steady-state TOF (after 360 min on stream) and % Pd ( $x$ ). Error bars were obtained from a minimum of two separate measurements using fresh catalysts. (C, D) Analogous plots when the catalytic data are normalized by considering only Pd surface sites as the active catalytic species.

analysis of the compositional dependence of the Pd<sub>x</sub>Au<sub>100-x</sub>NPs in comparison to PXRD data (using Vegard's law) is also presented for comparison in Figure S10 in the Supporting Information.

XPS also provides valuable information relating to the distribution of oxidation states of the observable metal atoms in the Pd<sub>x</sub>Au<sub>100-x</sub>NPs. It is expected that subsurface atoms in metallic NPs will be zerovalent, while a proportion of surface (or near-surface) atoms may be oxidized in their native state. Following the premise that XPS is somewhat surface sensitive in the analysis of the Pd<sub>x</sub>Au<sub>100-x</sub>NPs, a clear trend was seen in the distribution of Pd(0) versus Pd(II) and Au(0) versus Au(I), as a function of  $x$  (Table S3 in the Supporting Information). For Pd-rich NPs, the Pd(II):Pd(0) ratio was significant (~1:3), while only Au(0) was detected. As the total amount of Au was increased, the relative signal for Pd(II) was diminished (becoming undetectable at  $x \leq 18$ ), accompanied by a continual increase in the intensity of the signal due to Au(I).

Individual Pd<sub>x</sub>Au<sub>100-x</sub>NPs were supported onto amorphous silica for catalytic studies (see section 2.3). The supported NPs were studied by high-resolution (HR)-TEM, and the fast Fourier transformations (FFT) of the acquired micrographs were used to measure the atomic lattice spacings corresponding to the  $\langle 111 \rangle$  planes (Figures S24–S33 in the Supporting Information). The HRTEM data indicate that the  $d$  spacings increased as a function of the relative Pd:Au composition, which agrees with the PXRD studies (Table S2 in the Supporting Information). This is expected, since the  $d$  spacings for pure metallic Pd and Au are 225 and 235 pm,<sup>68</sup> respectively. 2-D EDS mapping of unsupported individual Pd<sub>59</sub>Au<sub>41</sub>NPs did not reveal any discernible core–shell segregation and indicated that individual NPs of intermediate composition were homogeneously alloyed (Figures S11 and S12 in the Supporting Information).

**2.3. Vapor-Phase Catalytic Hydrogenation by Pd<sub>x</sub>Au<sub>100-x</sub>NPs.** With a series of highly defined PdAuNPs in hand, model catalytic studies were conducted to probe the relationship between composition and surface reactivity. We chose to conduct model catalytic studies using gas-phase reactions, because valuable kinetic reactivity information can be obtained in this regime. This type of “on-stream” information cannot easily be obtained via liquid-phase batch reaction studies. Moreover, complications that are inherent to liquid-

phase reactions (e.g., leaching of catalytically active metal atoms or clusters from the NP surfaces into solution) are nonexistent in the gas phase. Specifically, we studied the continuous gas-phase hydrogenation of cyclohexene (CHE) by H<sub>2</sub>. This is a simple yet ideal model reaction of industrial relevance, which also provides information directly related to NP surface binding strengths toward reactants and products. To achieve these goals, composite catalysts were first prepared by incipient wetness deposition of the preformed PVP-capped Pd<sub>x</sub>Au<sub>100-x</sub>NPs onto amorphous support media. This process was conducted to obtain composites with 1–2 wt % target loading of total metal. Silica was utilized in the first instance, because it is not chemically reactive and does not induce strong metal–support interactions (SMSI) that may otherwise alter the NP morphologies and/or compositions.<sup>69–73</sup> It should be noted that all of the catalysts were used directly as synthesized after washing and drying at 70 °C; it is therefore assumed that some (or all) of the PVP capping agents remained on the NPs. High-temperature pretreatment (e.g., calcination) was not employed in any instance; the catalysts were highly active after 30 min of on-stream H<sub>2</sub>/He purging at 25 °C, prior to introduction of CHE vapor. It is known from several previous studies that PVP is released from the NP surfaces under a reducing environment; it is also permeable enough to permit adsorbates to access the reactive surface atoms.<sup>74</sup>

In all of our studies, a CHE/H<sub>2</sub> mixture of known molar concentration was flowed across a bed consisting of the SiO<sub>2</sub>-supported Pd<sub>x</sub>Au<sub>100-x</sub>NPs with real-time monitoring of the effluent gas by gas chromatography (GC). Activity data was then converted into normalized turnover frequencies (TOFs; see the Supporting Information) per total metal surface sites per second. The normalized TOFs for a series of SiO<sub>2</sub>-supported Pd<sub>x</sub>Au<sub>100-x</sub>NPs with varying values of  $x$  are shown in Figure 5A, and the trend in dependence of TOF versus  $x$  is shown in the inset Figure 5B. The data in Figures 5A,B have been normalized on the basis of total NP surface area, regardless of atomic identity (Pd or Au). This approach is useful because it negates the potential effects of enrichment of one metal at (or near) the NP surfaces under the reducing reaction conditions. An alternative normalization treatment of the data that considers only Pd surface sites as active catalytic species is also provided for comparative purposes, in Figure 5C,D. The trend in catalyst

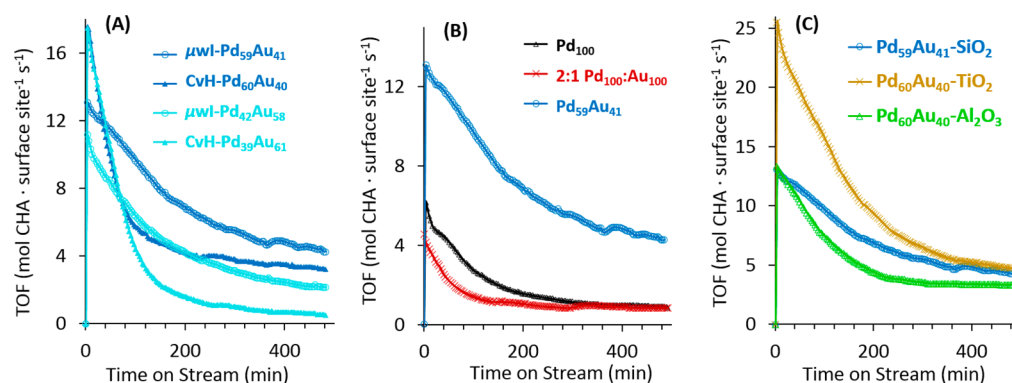


**Figure 6.** (A) Comparison of catalyst activity based on the synthetic heating method for the two most active catalyst compositions. (B) Comparison of normalized TOFs for the most active  $\mu$ wl-prepared alloy catalyst versus pure PdNPs and a 1:1 physical mixture of PdNPs and AuNPs. (C) Investigation of potential support-mediated effects upon catalytic activity.

activity as a function of  $x$  is the same for both treatments; only the absolute steady-state TOF values differ.

In general, all catalysts showed high initial hydrogenation activity upon exposure to CHE, forming cyclohexane CHA as the sole product and reaching steady-state turnover rates after 4–5 h. This behavior is common for such catalysts because higher energy facets which provide the most reactive surface sites on the NPs are more rapidly rearranged and/or poisoned. The resulting catalysts were then stable over many hours and also upon recycling (Figures S45–S59 in the Supporting Information). It is immediately obvious from the data that Pd-rich NPs were the most reactive catalysts. This is to be expected, since Au is unable to oxidatively add  $H_2$  under these reaction conditions. A catalyst consisting of pure AuNPs prepared using the same  $\mu$ wl method was completely inactive in CHE hydrogenation (Figures S4A,C, gold triangles). More interestingly, a pure PdNP-based catalyst gave TOF = 1.02 mol of CHA (surface site) $^{-1}$  s $^{-1}$  after 6 h on stream, while all catalysts with  $x \geq 42$  gave significantly higher steady-state turnovers. This is direct evidence for the synergistic behavior of Pd and Au when intrinsically alloyed. The best catalyst was found to be of composition Pd<sub>59</sub>Au<sub>41</sub>, having a TOF = 4.69 mol of CHA (total metal surface site) $^{-1}$  s $^{-1}$ , also after 6 h on stream. The overall trend in steady-state TOF versus NP composition gives a curve that has a single maximum in activity  $x =$  ca. 59 (Figure 5B,D). While all Pd-rich NPs showed some degree of activity, steady-state, Au-rich catalysts with  $x < 27$  were inactive after only 1 h. Au-rich NPs (particularly Pd<sub>27</sub>Au<sub>73</sub> and Pd<sub>18</sub>Au<sub>82</sub>) were quite reactive initially but underwent rapid deactivation to low but stable steady-state TOF values. One plausible explanation for this behavior is that Au-rich PdAuNPs will initially have a larger proportion of Pd<sub>1</sub>Au<sub>2</sub> ensembles that are highly active and also therefore unstable, thus undergoing rapid deactivation (via restructuring or passivation events). Temperature-dependent TOF values were used to derive activation energies for the CHE hydrogenation reaction, which were in the range 33.4–42.2 kJ mol $^{-1}$  (Figure S64 in the Supporting Information).

Rebelli et al. have studied the rate of propene hydrogenation by SiO<sub>2</sub>-supported PdNPs, as a function of deposition of differing amounts of randomly deposited Au overlayers.<sup>75</sup> Interestingly, they found that the most reactive catalysts were obtained using 0.6–0.9 monolayer of Au. This seems to suggest their “postsynthetic” preparation method for PdAu nanocatalysts resulted in different proportions of Pd<sub>*x*</sub>Au<sub>*y*</sub> ensembles as active surface sites; meanwhile, this route does not result in

intrinsic Pd–Au alloying of the NP subsurface, which may also have important ramifications for surface reactivity.<sup>75</sup>

Having confirmed that Pd<sub>*x*</sub>Au<sub>100–*x*</sub>NPs with slightly Pd rich compositions appeared to be the most active species in CHE hydrogenation, we then prepared a smaller series of catalysts with the same compositions, but using CvH. Interestingly, these catalysts exhibited significantly lower steady-state TOF values under identical reaction conditions (Figure 6A). We have observed this type of behavior in the past when comparing pure RhNPs prepared by  $\mu$ wl and CvH. The potential origins of this behavior are discussed in section 2.5. Another important control study was performed to assess whether the synergistic effect upon hydrogenation reactivity is due to the intrinsic alloying of Pd and Au atoms within the same NPs. An SiO<sub>2</sub>-supported catalyst was prepared by deposition of pure PdNPs and AuNPs in a 2:1 molar ratio. The NPs were not aggregated (Figure S60 in the Supporting Information), and it can be reasonably assumed that the NPs were randomly mixed throughout the material. The CHE hydrogenation activity for this catalyst at steady state was closely matched with that for the catalyst containing only PdNPs (Figure 6B). This confirms not only that atomic-level alloying of Pd and Au is critical but also that AuNPs do not perform any noticeable synergistic function in the presence of PdNPs (e.g., spillover effects). Finally, we performed a study to check for the potential role of the SiO<sub>2</sub> supports upon catalysis. For many well-known reaction involving substrates more chemically complex than CHE, support interactions may greatly affect the product selectivity. The simple CHE hydrogenation reaction should not be affected by support effects, itself therefore acting as a conveniently selective probe for the reactivity of the NP surfaces. Indeed, when the most active hydrogenation catalysts ( $\mu$ wl-Pd<sub>59</sub>Au<sub>41</sub>NPs) were deposited on amorphous  $\gamma$ -alumina (Al<sub>2</sub>O<sub>3</sub>) and titania (TiO<sub>2</sub>) and tested as CHE hydrogenation catalysts, there was no obvious difference in the steady-state TOFs in comparison to SiO<sub>2</sub>-anchored NPs (Figure 6C). Only the initial TOF values for the TiO<sub>2</sub>-supported NPs were significantly higher than those previously observed, but this was most likely due to slight differences in the morphologies of the as-synthesized NPs.

**2.4. Theoretical Assessment of Pd<sub>*x*</sub>Au<sub>100–*x*</sub>NP Compositional Dependence in Catalytic Hydrogenation.** The most active catalyst composition identified for CHE hydrogenation is very close to the 2:1 Pd:Au ratio that is favored in industrial processes.<sup>34,76</sup> Oxidative cleavage of H<sub>2</sub> to give two H atoms is an important rate-determining step in the hydro-

genation reaction. However, the measured activation energies for the alloy catalysts were the same as those for the pure PdNP-based catalyst. It is clear that Pd atoms are responsible for H<sub>2</sub> activation in all instances, confirmed by the fact that Au-rich alloy catalysts and pure AuNPs were completely catalytically inactive. A plausible explanation for these trends in overall reactivity is that the presence of an optimal amount of Au at the NP surfaces assists in desorption of the CHA products, resulting in more vacant surface sites for further hydrogenation reactions. This hypothesis can be addressed in detail using DFT to study the electronic structure of PdAu alloys as a function of relative composition.

Garcia and Zhang reported that the H binding energy can be used as a reaction descriptor to understand the catalytic activity trend of CHE hydrogenation.<sup>38</sup> On the basis of the scaling between reaction intermediates, the minimum overall free energy that needs to be overcome along the reaction path was found at an optimal hydrogen binding energy:  $\Delta E_{\text{H}^*} = -0.4$  eV. In this work we have followed the same framework and used the H binding energy on Au/Pd random alloy surfaces to understand the activity trends observed experimentally. Figure 7 shows the average H binding energy at different Pd alloying

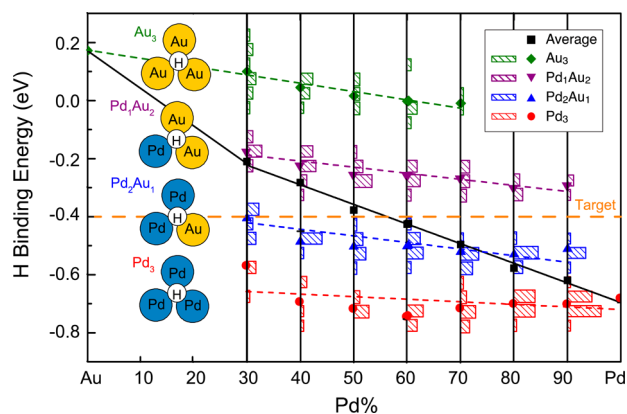


**Figure 7.** Decomposition of the average H binding energy into an ensemble of specific sites determined by the number of Au vs Pd atoms at the binding site. The bars indicate the frequency of different binding energies at the seven compositions; the solid symbols indicate the average binding energy per site. The target H binding, at  $-0.4$  eV, is highlighted by the orange dashed line.

ratios. The average H binding energy (black solid line) varies nearly linearly with the Pd alloying ratio from 30 to 100% and reaches the target H binding  $\Delta E_{\text{H}^*} = -0.4$  eV (orange dashed line) at a percent Pd between 50 and 60%, in good agreement with our experiments.

Due to the large disparity of H binding to Au and Pd atoms, it is also important to consider H binding at different ensembles ( $\text{Au}_3$ ,  $\text{Au}_2\text{Pd}_1$ ,  $\text{AuPd}_2$ , and  $\text{Pd}_3$ ; Figure 7, inset). For each intermediate alloy composition, the average binding energy is decomposed into individual histograms of the binding sites mentioned above. Among these four ensembles,  $\text{Au}_3$  binds H too weakly to be reactive, while  $\text{Pd}_3$  binds H binding so strongly that the sites will be poisoned. In contrast, both  $\text{Au}_2\text{Pd}_1$  and  $\text{AuPd}_2$  are close to the target H binding and are expected to be active in the catalytic system. With an assumption that both Pd and Au are randomly distributed, compositions with percent Pd between 50% and 60% have more  $\text{Au}_2\text{Pd}_1$  and  $\text{AuPd}_2$  ensembles on the surfaces, thus creating more active sites to drive the reaction.

Furthermore, these experimental and theoretical results provided us an opportunity to validate our previous model for CHE hydrogenation as a function of the type of precious metal(s) present.<sup>38</sup> The volcano plot (Figure 8) shows the

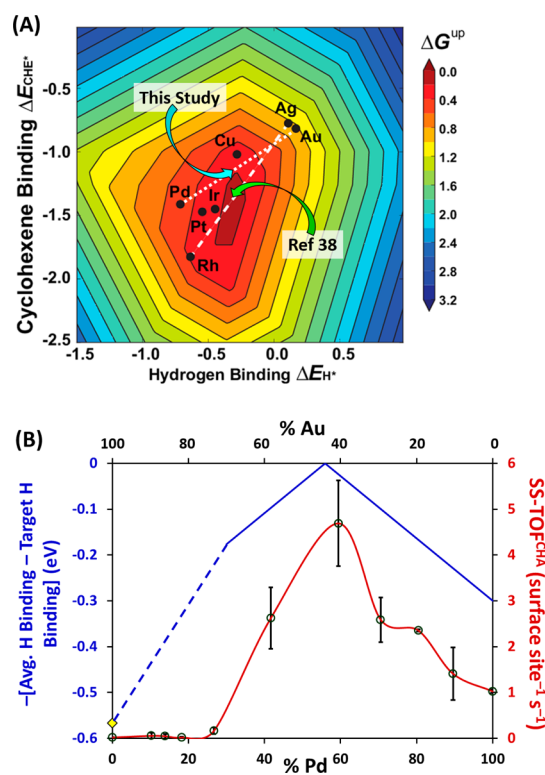


**Figure 8.** (A) Volcano contour plot of the free energies ( $\Delta G^{\text{up}}$ ) for H and CHE binding calculated for individual noble metals. Alloys of two metals with varying compositions are expressed as lines joining the points between the pure metals. (B) Deviation in binding energies along the dotted line adjoining Pd and Au in (A) shown in blue. This was found by calculating the difference in the average H binding energy versus the target H binding energy ( $-0.4$  eV). The calculated deviation for pure Au is  $-0.576$  eV. For comparison, the experimentally observed steady-state turnover values from Figure 5B are shown in red.

predicted positions of individual metals as a function of the CHE and H binding energies; Au weakly binds both species and Pd binds both more strongly, but neither lie near the center of the volcano, at which point reactant adsorption and product desorption can be considered optimized. However, the line joining the two extremes (for 100% Pd and 100% Au; dotted line, Figure 8A) should predict the CHE hydrogenation activity as a function of  $x$  in our  $\text{Pd}_x\text{Au}_{100-x}$ NPs. Unlike our previous work with RhAgNPs of varying composition (dashed line, Figure 8A), the line between Pd and Au never passes through the center of the volcano; correspondingly, the measured TOFs for CHE hydrogenation by PdAuNPs are globally lower than for RhAgNPs. Nonetheless, the predicted maximum activity and the general shape of the reactivity curve are in very good agreement with the experimental data (Figure 8B).

**2.5. Solution-State <sup>1</sup>H NMR Quantification of PVP Incorporation in PdAuNPs.** In this work, and in previous studies of other noble-metal NPs,<sup>38</sup> we have found that the normalized TOFs are consistently higher for  $\mu\text{wI}$ -prepared catalysts in comparison to their CvH-prepared counterparts, under identical catalyst pretreatment conditions. One obvious

explanation for this interesting phenomenon is that the  $\mu$ wI method somehow incorporates less PVP polymer into the products, thus resulting in a larger proportion of substrate-accessible surface sites per NP. In this work, we have attempted to directly address this question using solution-state  $^1\text{H}$  NMR techniques to quantify the amount of PVP incorporated as a function of the heating method.<sup>77–80</sup> To begin,  $^1\text{H}$ -DOSY experiments were conducted to confirm that all PVP was physically attached to the  $\text{Pd}_{59}\text{Au}_{41}$ NPs and that the prior isolation and purification steps had removed all excess (unbound) PVP chains. DOSY is useful in distinguishing between bound and free PVP chains by monitoring the differences in the chemical environments of H atoms on the pyrrolidone rings and the alkyl backbone, as a function of proximity to the NP surfaces. PVP monomers within the same NP-bound chains are in rapid dynamic exchange at a rate that is not observable on the NMR time scale. Therefore, DOSY cannot distinguish between PVP monomers that are directly in contact with a NP surface versus neighboring monomers of the same chains that are folded or looped around the NP in a globular fashion. Weighted  $^1\text{H}$ -DOSY analysis of the PVP-capped  $\mu$ wI- $\text{Pd}_{59}\text{Au}_{41}$ NPs suspended in  $\text{CDCl}_3$  yielded an average diffusion coefficient of  $5 \times 10^{-10} \text{ m}^2 \text{ s}^{-1}$  (Figure S69 in the Supporting Information). In comparison, the  $^1\text{H}$ -DOSY spectrum for a control solution of the same concentration of free PVP in  $\text{CDCl}_3$  (in the absence of any NPs) revealed a larger diffusion coefficient of  $7 \times 10^{-10} \text{ m}^2 \text{ s}^{-1}$  (Figure S70 in the Supporting Information). The spin–lattice relaxation times ( $T_1$ ) obtained for the H atoms in different chemical environments were approximately 1 s. The value of the spin–spin relaxation time ( $T_2$ ) was 39 times less than  $T_1$ .

On the basis of the above values, PVP quantification by solution state  $^1\text{H}$  NMR was performed using a relaxation delay,  $d_1 = 30 \text{ s}$ , to ensure complete relaxation of all PVP-H atoms. 4,4'-Bipyridine was chosen as an internal standard; the inherent symmetry of this molecule simplifies its spectrum to only two sets of peaks that occur far upfield from the region of interest. The areas under the peaks arising due to the H atoms of bound PVP were integrated for two samples prepared by the different heating methods, denoted as  $\mu$ wI- $\text{Pd}_{59}\text{Au}_{41}$  and CvH- $\text{Pd}_{60}\text{Au}_{40}$ NPs. These values were then scaled against the peak area values for the internal standard (of known concentration). This enabled us to obtain values for the concentration of PVP in the two PdAuNP samples. The weight percent of PVP for the  $\mu$ wI-prepared NPs was 88%, and the corresponding value for the CvH-prepared NPs was 92%. These values are reasonable, since, under standard synthesis conditions, 15 mg of total metal (Pd + Au) and excess PVP resulted in the isolation of 75–100 mg of PVP-capped PdAuNP products. The values were then normalized to account for slight differences in average NPs size between the two samples, to allow for a direct comparison of the average number of PVP monomers incorporated per surface atom. Ultimately, this yielded values of 17.9 PVP monomers per surface atom for the  $\mu$ wI- $\text{Pd}_{59}\text{Au}_{41}$ NPs and 27.6 PVP monomers per surface atom for the CvH- $\text{Pd}_{60}\text{Au}_{40}$ NPs (Table S4 in the Supporting Information). These values correspond to approximately 5.6 and 8.6 PVP chains per NP, respectively ( $\text{PVP}_{(\text{MW})} = 58000 \text{ amu}$ ; corresponding to 522 monomers per chain). It is clear from these results that significantly more PVP was indeed incorporated into the CvH-prepared NPs. Therefore, it is reasonable to assume that the superior catalytic activity observed for the  $\mu$ wI-PdAuNPs is due, at least in part, to

more easily accessible NP surface sites. However, the differences in catalytic performance as a function of heating method may also be partially caused by other, more subtle factors (e.g., differences in NP morphology, surface chemical composition, or crystallinity).

**2.6. Conclusions.** Small  $\text{Pd}_x\text{Au}_{100-x}$ NPs with defined size and randomly alloyed structures can be prepared under microwave-assisted heating and utilized as model catalysts to investigate reactivity as a function of relative metal composition. Catalysts with compositions close to  $\text{Pd}_{60}\text{Au}_{40}$  were experimentally found to be most proficient in vapor-phase alkene hydrogenation at 298 K. Under the assumption that the Pd and Au atoms are distributed randomly on the surfaces of the PdAuNPs, DFT calculations showed that the catalytic performance was nearly linearly related to the Pd alloy ratio from 30 to 100%. The optimal composition is between  $\text{Pd}_{50}\text{Au}_{50}$  and  $\text{Pd}_{60}\text{Au}_{40}$ , which is consistent with experimental results. The activities of microwave-prepared PdAuNPs were found to be consistently significantly higher than those of conventionally prepared catalysts with comparable compositions. Quantitative NMR studies of the catalyst materials indicated that less PVP polymer capping agent was incorporated into the microwave-synthesized PdAuNPs, which is likely to be an important factor in controlling the proportion of accessible surface sites available for catalysis.

### 3. EXPERIMENTAL SECTION

**3.1. Synthesis of  $\sim 2.5 \text{ nm Pd}_x\text{Au}_{100-x}$ NPs.** PdAuNPs were prepared using the following general procedure. All  $\mu$ wI reactions were performed in a MARS microwave reactor (CEM Corp.) operating with fiber-optic temperature feedback control ( $\pm 0.1^\circ\text{C}$ ) and magnetic stirring (450 rpm), with the reaction vessel open to air (see the Supporting Information for further details). CvH experiments were conducted using the exact same arrangement of apparatus but with heating and stirring provided by a conventional hot plate/stirrer via immersion of the reaction flask in a silicon oil bath. PVP ( $\text{MW} = 58000$ , 20 equiv of monomers per mmol of Pd + Au precursors) and  $\text{NaBH}_4$  (5.6 equiv per Au(III)) were dissolved in EG (15.0  $\text{cm}^3$ , 99.8%), and the solution temperature was brought to  $150^\circ\text{C}$ . Separately, the metal precursors ( $\text{K}_2\text{PdCl}_4$ , 99%;  $\text{HAuCl}_4 \cdot 3\text{H}_2\text{O}$ , 98%) were each dissolved in EG (1.25  $\text{cm}^3$ ) and briefly sonicated to ensure complete dissolution. The exact molar amounts of each metal precursor employed in a given reaction were determined by the target value of  $x$  for the  $\text{Pd}_x\text{Au}_{100-x}$ NPs; the combined molar amount of Pd(II) and Au(III) precursors was always 0.10 mmol. The two solutions were then combined and mixed to give a total volume of 2.5  $\text{cm}^3$ , which was delivered directly into the hot PVP/ $\text{NaBH}_4$  solution (via disposable PTFE tubing, i.d. 1.0 mm) at a rate of  $300 \text{ cm}^3 \text{ h}^{-1}$  (12 mmol  $\text{h}^{-1}$ ), controlled by a programmable syringe pump (WPI, Inc.). After the addition was complete (30 s), the reaction mixture was stirred under constant heating for a further time,  $t$ . At the end of the reaction ( $t + 30 \text{ s}$ ), the reaction flask was quickly cooled using an ice–water bath. The resulting  $\text{Pd}_x\text{Au}_{100-x}$ NPs were purified in a two-stage process. First, the products were precipitated by addition of excess acetone (ca. 75  $\text{cm}^3$ ) and isolated by ultracentrifugation (5.5 krpm, 300 s). To remove excess PVP, the solids were then redispersed in ethanol (ca. 15  $\text{cm}^3$ ), reprecipitated by addition of excess hexanes (ca. 75  $\text{cm}^3$ ), and isolated by centrifugation. The NPs were then stored in air, either as dry glassy solids or as suspensions in ethanol.

**3.2. Growth of Larger Pd<sub>50</sub>Au<sub>50</sub>NPs.** To synthesize larger PdAuNPs, the ~2.5 nm particles obtained by the method described above were used directly, without isolation. After  $t = 300$  s, a second solution containing a 1:1 molar mixture of Pd(II) and Au(III) precursors was injected into the existing reaction, at a slower rate of  $20 \text{ cm}^3 \text{ h}^{-1}$  ( $0.80 \text{ mmol h}^{-1}$ ) under continuous  $\mu\text{wI}$  at  $150^\circ\text{C}$ . The amount of additional reagents added was determined by the target PdAuNP size. After the second injection was complete (450 s), the reaction mixture was stirred for a further 300 s, followed by isolation of the products as described above.

**3.3. Catalyst Preparation and Hydrogenation Studies.** The catalysts were prepared by direct deposition of 5–8 mg amounts of the PVP-capped Pd<sub>x</sub>Au<sub>100-x</sub>NPs, PdNPs, or AuNPs onto precalcined amorphous silica (particle dimensions ~1–6  $\mu\text{m}$ ),<sup>37</sup> to achieve a target of approximately 1.5 wt % total metal loading. Pure PdNPs and AuNPs were prepared using the same  $\mu\text{wI}$ -assisted method as that described above. Typically, NPs were suspended in water/ethanol (9.0  $\text{cm}^3$ , 4/5 v/v) and sonicated for 5 min to ensure a homogeneous dispersion. Separately, SiO<sub>2</sub> (100 mg) was rapidly stirred in water/ethanol (9.0  $\text{cm}^3$ , 5/4 v/v) in a 20  $\text{cm}^3$  glass scintillation vial containing a micro magnetic stirrer bar. NP suspensions were then added dropwise over 10 min. The resulting slurries were stirred for another 10 min and sonicated for 10 min, and this cycle was repeated at least two more times (or until the supernatant was colorless). The composite catalysts were isolated by vacuum filtration in air, washed copiously with water and ethanol, and finally dried overnight in an oven at  $70^\circ\text{C}$ . The actual resulting weight percent of Pd + Au loading for each catalyst was measured by digestion of a small amount (~2 mg) in aqua regia (10  $\text{cm}^3$ ) and analysis by ICP-MS.

For vapor-phase hydrogenation studies, a small amount of a given NP-SiO<sub>2</sub> catalyst (2–6 mg) was diluted by physical mixing with acid-washed and precalcined sand (100 mg) and loaded into a custom-made quartz U-tube, suspended above a D3-porosity frit. The sample was held constant at the desired reaction temperature using a water bath and circulator. The remainder of the quartz reactor line was heated to  $\sim 90^\circ\text{C}$ , and the entire line and catalyst bed were purged with the reactant gas mixture (H<sub>2</sub>/He 1/1) for 30 min prior to the introduction of the alkene reactant. CHE was introduced to the gas flow via an in-line saturator fitted with a fritted bubbler. The purity of CHE (anhydrous,  $\geq 99\%$ ) was verified prior to use by <sup>1</sup>H and <sup>13</sup>C{<sup>1</sup>H} NMR spectroscopy. Activity data were obtained by automated (pneumatically gated) continuous sampling of the product flow, which was directed into an HP Agilent 6890 GC fitted with a Restex Stabiliwax column ( $l = 15 \text{ m}$ ) and tandem flame ionization and thermal conductivity detectors (FID and TCD, respectively). Activity and turnover frequency (TOF) values were obtained on the basis of estimated surface area to volume ratios (obtained from TEM). Activation energies were determined from Arrhenius plots of steady-state activity values at five temperatures (6, 12, 18, 24, and  $30^\circ\text{C}$ ); see the [Supporting Information](#) for further details.

**3.4. Computational Methods.** H binding energies on Au/Pd random alloy NPs were calculated using DFT implemented in the VASP code.<sup>81</sup> Core electrons were described with the projector augmented-wave method.<sup>82,83</sup> Electron correlation was evaluated within the generalized gradient approximation using the Perdew–Wang 91 (PW91).<sup>84,85</sup> Kohn–Sham wave functions for the valence electrons were expanded in a plane wave basis set with an energy cutoff of 300 eV.<sup>86,87</sup>

Convergence of our calculations was tested by increasing the energy cutoff to 400 eV, and H binding energies of Au(111) and Pd(111) were found to vary by less than 0.01 eV. Spin polarization was tested and used as required.

H binding energies were calculated on the (111) surface of a four-layer,  $4 \times 4$  unit cell, face centered cubic (FCC) surface. According to the experimental results ([Figure 5](#)), alloys of Au/Pd were considered with the following compositions: Au<sub>10</sub>Pd<sub>90</sub>, Au<sub>20</sub>Pd<sub>80</sub>, Au<sub>30</sub>Pd<sub>70</sub>, Au<sub>40</sub>Pd<sub>60</sub>, Au<sub>50</sub>Pd<sub>50</sub>, Au<sub>60</sub>Pd<sub>40</sub>, and Au<sub>70</sub>Pd<sub>30</sub>. For each composition, eight random alloy configurations were generated, and for each configuration, the H binding energy on four FCC hollow sites was calculated to obtain the average H binding energy for each alloy composition (32 total binding sites). The selections of hollow sites were all in the similar proportions of Au and Pd in the slab surfaces. The H binding energy was referenced to the H<sub>2</sub> molecule under vacuum. A vacuum of at least 12 Å was used to separate periodic images between slabs. The Brillouin zone was sampled with a  $3 \times 3 \times 1$  Monkhorst–Pack  $k$ -point mesh and integrated using the method of Methfessel and Paxton.<sup>88,89</sup> All atoms in the nanoparticle were allowed to relax; geometries were considered optimized when the force on each atom was  $<0.01 \text{ eV/\AA}$ .

## ■ ASSOCIATED CONTENT

### ● Supporting Information

The Supporting Information is available free of charge on the [ACS Publications website](#) at DOI: [10.1021/acscatal.6b01014](https://doi.org/10.1021/acscatal.6b01014).

Additional TEM, PXRD, 2D-EDS, HRTEM, XPS, and UV/vis characterization data for the NPs, further experimental details, NMR spectra and details of the PVP quantification studies, and additional theoretical information ([PDF](#))

## ■ AUTHOR INFORMATION

### Corresponding Authors

\*E-mail for G.H.: [henkelman@cm.utexas.edu](mailto:henkelman@cm.utexas.edu).

\*E-mail for S.M.H.: [smh@cm.utexas.edu](mailto:smh@cm.utexas.edu).

### Present Addresses

<sup>§</sup>Department of Chemistry, University of Minnesota, Minneapolis, MN 55455, USA.

<sup>||</sup>Department of Chemical Engineering, Stanford University, Stanford, CA 94305, USA.

### Notes

The authors declare no competing financial interest.

## ■ ACKNOWLEDGMENTS

The authors wish to thank Dr. Dwight Romanovicz (UT Austin; TEM), Dr. Hugo Celio (UT Austin; XPS), Dr. Steven Sorey and Dr. Angela Spangenberg (UT Austin; NMR), and Dr. Vincent M. Lynch (UT Austin; PXRD) for analytical assistance. Funding for this research was provided by the National Science Foundation under award number CHE-1505135, the Welch Foundation (F-1738 & F-1841), and the Texas Higher Education Coordinating Board (003658-0008-2013).

## ■ REFERENCES

- (1) Climent, M. J.; Corma, A.; Iborra, S. *Chem. Rev.* **2011**, *111*, 1072–1133.
- (2) Prins, R.; De Beer, V. H. J.; Somorjai, G. A. *Catal. Rev.: Sci. Eng.* **1989**, *31*, 1–41.

- (3) Xia, Y.; Yang, P.; Sun, Y.; Wu, Y.; Mayers, B.; Gates, B.; Yin, Y.; Kim, F.; Yan, H. *Adv. Mater.* **2003**, *15*, 353–389.
- (4) Buck, M. R.; Bondi, J. F.; Schaak, R. E. *Nat. Chem.* **2011**, *4*, 37–44.
- (5) Ferrando, R.; Jellinek, J.; Johnston, R. L. *Chem. Rev.* **2008**, *108*, 845–910.
- (6) Gao, F.; Goodman, D. W. *Chem. Soc. Rev.* **2012**, *41*, 8009–8020.
- (7) Vasquez, Y.; Sra, A. K.; Schaak, R. E. *J. Am. Chem. Soc.* **2005**, *127*, 12504–12505.
- (8) Lim, B.; Jiang, M.; Camargo, P. H.; Cho, E. C.; Tao, J.; Lu, X.; Zhu, Y.; Xia, Y. *Science* **2009**, *324*, 1302–1305.
- (9) Kusada, K.; Kobayashi, H.; Ikeda, R.; Kubota, Y.; Takata, M.; Toh, S.; Yamamoto, T.; Matsumura, S.; Sumi, N.; Sato, K.; Nagaoka, K. *J. Am. Chem. Soc.* **2014**, *136*, 1864–1871.
- (10) Zhang, H.; Jin, M.; Xia, Y. *Chem. Soc. Rev.* **2012**, *41*, 8035–8049.
- (11) Kusada, K.; Yamauchi, M.; Kobayashi, H.; Kitagawa, H.; Kubota, Y. *J. Am. Chem. Soc.* **2010**, *132*, 15896–15898.
- (12) Goodenough, J. B.; Manoharan, R.; Shukla, A. K.; Ramesh, K. V. *Chem. Mater.* **1989**, *1*, 391–398.
- (13) Park, K.-W.; Choi, J.-H.; Kwon, B.-K.; Lee, S.-A.; Sung, Y.-E.; Ha, H.-Y.; Hong, S.-A.; Kim, H.; Wieckowski, A. J. *Phys. Chem. B* **2002**, *106*, 1869–1877.
- (14) Link, S.; Wang, Z. L.; El-Sayed, M. A. *J. Phys. Chem. B* **1999**, *103*, 3529–3533.
- (15) Strasser, P.; Koh, S.; Anniyev, T.; Greeley, J.; More, K.; Yu, C. F.; Liu, Z. C.; Kaya, S.; Nordlund, D.; Ogasawara, H.; Toney, M. F. *Nat. Chem.* **2010**, *2*, 454–460.
- (16) Yu, W. Y.; Mullen, G. M.; Flaherty, D. W.; Mullins, C. B. *J. Am. Chem. Soc.* **2014**, *136*, 11070–11078.
- (17) Ham, H. C.; Hwang, G. S.; Han, J.; Nam, S. W.; Lim, T. H. *J. Phys. Chem. C* **2010**, *114*, 14922–14928.
- (18) Slanac, D. A.; Hardin, W. G.; Johnston, K. P.; Stevenson, K. J. *J. Am. Chem. Soc.* **2012**, *134*, 9812–9819.
- (19) Cui, C.; Gan, L.; Heggen, M.; Rudi, S.; Strasser, P. *Nat. Mater.* **2013**, *12*, 765–771.
- (20) Chen, S.; Ferreira, P. J.; Sheng, W. C.; Yabuuchi, N.; Allard, L. F.; Shao-Horn, Y. *J. Am. Chem. Soc.* **2008**, *130*, 13818–13819.
- (21) Wanjala, B. N.; Luo, J.; Loukrakpam, R.; Mott, D.; Njoki, P. N.; Fang, B.; Engelhard, M.; Naslund, H. R.; Wu, J. K.; Wang, L.; Malis, O.; Zhong, C.-J. *Chem. Mater.* **2010**, *22*, 4282–4294.
- (22) Chen, M.; Kumar, D.; Yi, C.-W.; Goodman, D. W. *Science* **2005**, *310*, 291–293.
- (23) Pritchard, J.; Kesavan, L.; Piccinini, M.; He, Q.; Tiruvalam, R.; Dimitratos, N.; Lopez-Sanchez, J. A.; Carley, A. F.; Edwards, J. K.; Kiely, C. J.; Hutchings, G. J. *Langmuir* **2010**, *26*, 16568–16577.
- (24) Mori, K.; Miura, Y.; Shironita, S.; Yamashita, H. *Langmuir* **2009**, *25*, 11180–11187.
- (25) Han, Y. F.; Zhong, Z.; Ramesh, K.; Chen, F.; Chen, L.; White, T.; Tay, Q.; Yaakub, S. N.; Wang, Z. *J. Phys. Chem. C* **2007**, *111*, 8410–8413.
- (26) Hou, W.; Dehm, N. A.; Scott, R. W. *J. Catal.* **2008**, *253*, 22–27.
- (27) Marx, S.; Baiker, A. *J. Phys. Chem. C* **2009**, *113*, 6191–6201.
- (28) Balcha, T.; Strobl, J. R.; Fowler, C.; Dash, P.; Scott, R. W. *ACS Catal.* **2011**, *1*, 425–436.
- (29) Wang, L.; Zhao, S.; Liu, C.; Li, C.; Li, X.; Li, H.; Wang, Y.; Ma, C.; Li, Z.; Zeng, J. *Nano Lett.* **2015**, *15*, 2875–2880.
- (30) Scott, R. W.; Datye, A. K.; Crooks, R. M. *J. Am. Chem. Soc.* **2003**, *125*, 3708–3709.
- (31) Yang, X.; Chen, D.; Liao, S.; Song, H.; Li, Y.; Fu, Z.; Su, Y. *J. Catal.* **2012**, *291*, 36–43.
- (32) Koenigsmann, C.; Sutter, E.; Adzic, R. R.; Wong, S. S. *J. Phys. Chem. C* **2012**, *116*, 15297–15306.
- (33) Liu, C. H.; Liu, R. H.; Sun, Q. J.; Chang, J. B.; Gao, X.; Liu, Y.; Lee, S. T.; Kang, Z. H.; Wang, S. D. *Nanoscale* **2015**, *7*, 6356–6362.
- (34) Dash, P.; Dehm, N. A.; Scott, R. W. *J. Mol. Catal. A: Chem.* **2008**, *286*, 114–119.
- (35) Gao, F.; Wang, Y.; Goodman, D. W. *J. Phys. Chem. C* **2009**, *113*, 14993–15000.
- (36) Gao, F.; Wang, Y.; Goodman, D. W. *J. Phys. Chem. C* **2010**, *114*, 4036–4043.
- (37) Dahal, N.; García, S.; Zhou, J.; Humphrey, S. M. *ACS Nano* **2012**, *6*, 9433–9446.
- (38) García, S.; Zhang, L.; Piburn, G. W.; Henkelman, G.; Humphrey, S. M. *ACS Nano* **2014**, *8*, 11512–11521.
- (39) Okamoto, H.; Massalski, T. B. *Bull. Alloy Phase Diagrams* **1985**, *6*, 229–235.
- (40) Kobayashi, H.; Yamauchi, M.; Ikeda, R.; Kitagawa, H. *Chem. Commun.* **2009**, *32*, 4806–4808.
- (41) Shan, B.; Wang, L.; Yang, S.; Hyun, J.; Kapur, N.; Zhao, Y.; Nicholas, J. B.; Cho, K. *Phys. Rev. B: Condens. Matter Mater. Phys.* **2009**, *80*, 035404.
- (42) Jette, E. R.; Foote, F. *J. Chem. Phys.* **1935**, *3*, 605–616.
- (43) Teranishi, T.; Miyake, M. *Chem. Mater.* **1998**, *10*, 594–600.
- (44) Voorhees, P. W. *J. Stat. Phys.* **1985**, *38*, 231–252.
- (45) Voorhees, P. W. *Annu. Rev. Mater. Sci.* **1992**, *22*, 197–215.
- (46) Belousov, O. V.; Belousova, N. V.; Sirotina, A. V.; Solov'yov, L. A.; Zhyzhaev, A. M.; Zharkov, S. M.; Mikhlin, Y. L. *Langmuir* **2011**, *27*, 11697–11703.
- (47) Galema, S. A. *Chem. Soc. Rev.* **1997**, *26*, 233–238.
- (48) Kappe, C. O. *Angew. Chem., Int. Ed.* **2004**, *43*, 6250–6284.
- (49) Daniel, M. C.; Astruc, D. *Chem. Rev.* **2004**, *104*, 293–346.
- (50) Jana, N. R.; Gearheart, L.; Murphy, C. J. *Adv. Mater.* **2001**, *13*, 1389–1392.
- (51) Jana, N. R.; Gearheart, L.; Murphy, C. J. *Langmuir* **2001**, *17*, 6782–6786.
- (52) Sra, A. K.; Schaak, R. E. *J. Am. Chem. Soc.* **2004**, *126*, 6667–6672.
- (53) Nikoobakht, B.; El-Sayed, M. A. *Chem. Mater.* **2003**, *15*, 1957–1962.
- (54) Xin, H. L.; Alayoglu, S.; Tao, R.; Genc, A.; Wang, C. M.; Kovarik, L.; Stach, E. A.; Wang, L. W.; Salmeron, M.; Somorjai, G. A.; Zheng, H. *Nano Lett.* **2014**, *14*, 3203–3207.
- (55) Kobayashi, H.; Yamauchi, M.; Kitagawa, H.; Kubota, Y.; Kato, K.; Takata, M. *J. Am. Chem. Soc.* **2010**, *132*, 5576–5577.
- (56) Lee, A. F.; Ellis, C. V.; Naughton, J. N.; Newton, M. A.; Parlett, C. M.; Wilson, K. *J. Am. Chem. Soc.* **2011**, *133*, 5724–5727.
- (57) Tao, F.; Grass, M. E.; Zhang, Y.; Butcher, D. R.; Renzas, J. R.; Liu, Z.; Chung, J. Y.; Mun, B. S.; Salmeron, M.; Somorjai, G. A. *Science* **2008**, *322*, 932–934.
- (58) Overbury, S. H.; Bertrand, P. A.; Somorjai, G. A. *Chem. Rev.* **1975**, *75*, 547–560.
- (59) Nashner, M. S.; Frenkel, A. I.; Somerville, D.; Hills, C. W.; Shapley, J. R.; Nuzzo, R. G. *J. Am. Chem. Soc.* **1998**, *120*, 8093–8101.
- (60) Anderson, R. M.; Zhang, L.; Loussaert, J. A.; Frenkel, A. I.; Henkelman, G.; Crooks, R. M. *ACS Nano* **2013**, *7*, 9345–9353.
- (61) Sahoo, B.; Nayak, N. C.; Samantaray, A.; Pujapanda, P. K. *Inorganic Chemistry*; PHI Learning: New Delhi, India, 2012.
- (62) Watts, J. F.; Wolstenholme, J. *An introduction to surface analysis by XPS and AES*; Wiley: New York, 2003; pp 12–13.
- (63) Personick, M. L.; Langille, M. R.; Zhang, J.; Mirkin, C. A. *Nano Lett.* **2011**, *11*, 3394–3398.
- (64) García, S.; Anderson, R. M.; Celio, H.; Dahal, N.; Dolocan, A.; Zhou, J.; Humphrey, S. M. *Chem. Commun.* **2013**, *49*, 4241–4243.
- (65) Tao, A. R.; Habas, S.; Yang, P. *Small* **2008**, *4*, 310–325.
- (66) Borodko, Y.; Humphrey, S. M.; Tilley, T. D.; Frei, H.; Somorjai, G. A. *J. Phys. Chem. C* **2007**, *111*, 6288–6295.
- (67) Panthi, B.; Mukhopadhyay, A.; Tibbitts, L.; Saavedra, J.; Pursell, C. J.; Rioux, R. M.; Chandler, B. D. *ACS Catal.* **2015**, *5*, 2232–2241.
- (68) Jana, D.; Dandapat, A.; De, G. *J. Phys. Chem. C* **2009**, *113*, 9101–9107.
- (69) Vayssilov, G. N.; Lykhach, Y.; Migani, A.; Staudt, T.; Petrova, G. P.; Tsud, N.; Skála, T.; Bruix, A.; Illas, F.; Prince, K. C.; Neyman, K. M. *Nat. Mater.* **2011**, *10*, 310–315.
- (70) Strayer, M. E.; Binz, J. M.; Tanase, M.; Kamali Shahri, S. M.; Sharma, R.; Rioux, R. M.; Mallouk, T. E. *J. Am. Chem. Soc.* **2014**, *136*, 5687–5696.

- (71) Liu, X.; Liu, M. H.; Luo, Y. C.; Mou, C. Y.; Lin, S. D.; Cheng, H.; Chen, J. M.; Lee, J. F.; Lin, T. S. *J. Am. Chem. Soc.* **2012**, *134*, 10251–10258.
- (72) Radnik, J.; Mohr, C.; Claus, P. *Phys. Chem. Chem. Phys.* **2003**, *5*, 172–177.
- (73) Vander Wal, R. L.; Ticich, T. M.; Curtis, V. E. *Carbon* **2001**, *39*, 2277–2289.
- (74) Tejamaya, M.; Römer, I.; Merrifield, R. C.; Lead, J. R. *Environ. Sci. Technol.* **2012**, *46*, 7011–7017.
- (75) Rebelli, J.; Detwiler, M.; Ma, S.; Williams, C. T.; Monnier, J. R. *J. Catal.* **2010**, *270*, 224–233.
- (76) Nishimura, S.; Ikeda, N.; Ebitani, K. *Catal. Today* **2014**, *232*, 89–98.
- (77) Morris-Cohen, A. J.; Malicki, M.; Peterson, M. D.; Slavin, J. W.; Weiss, E. A. *Chem. Mater.* **2013**, *25*, 1155–1165.
- (78) Kalyuzhny, G.; Murray, R. W. *J. Phys. Chem. B* **2005**, *109*, 7012–7021.
- (79) Malicki, M.; Knowles, K. E.; Weiss, E. A. *Chem. Commun.* **2013**, *49*, 4400–4402.
- (80) Moreels, I.; Fritzinger, B.; Martins, J. C.; Hens, Z. *J. Am. Chem. Soc.* **2008**, *130*, 15081–15086.
- (81) Kresse, G.; Hafner, J. *Phys. Rev. B: Condens. Matter Mater. Phys.* **1993**, *47*, 558–561.
- (82) Blöchl, P. E. *Phys. Rev. B: Condens. Matter Mater. Phys.* **1994**, *50*, 17953–17979.
- (83) Kresse, G.; Joubert, D. *Phys. Rev. B: Condens. Matter Mater. Phys.* **1999**, *59*, 1758–1775.
- (84) Perdew, J. P.; Chevary, J. A.; Vosko, S. H.; Jackson, K. A.; Pederson, M. R.; Singh, D. J.; Fiolhais, C. *Phys. Rev. B: Condens. Matter Mater. Phys.* **1992**, *46*, 6671–6687.
- (85) Perdew, J. P.; Chevary, J. A.; Vosko, S. H.; Jackson, K. A.; Pederson, M. R.; Singh, D. J.; Fiolhais, C. *Phys. Rev. B: Condens. Matter Mater. Phys.* **1993**, *48*, 4978.
- (86) Hohenberg, P.; Kohn, W. *Phys. Rev.* **1964**, *136*, B864–B871.
- (87) Kohn, W.; Sham, L. J. *Phys. Rev.* **1965**, *140*, A1133–A1138.
- (88) Monkhorst, H. J.; Pack, J. D. *Phys. Rev. B* **1976**, *13*, 5188–5192.
- (89) Methfessel, M.; Paxton, A. T. *Phys. Rev. B: Condens. Matter Mater. Phys.* **1989**, *40*, 3616–3621.